Faraday Discussions

Cite this: DOI: 10.1039/d5fd00092k

PAPER

Morphological, structural and compositional evolution of PtPdFeCoNi high-entropy alloy nanoparticles towards bifunctional oxygen electrocatalysis

Priya Jain,*[a] Pouya Hosseini,[a] Aleksander Kostka,[b] Eko Budiyanto,[c] Patrick Diehl,[d] Martin Muhler,[d] Harun Tüysüz,[cf] Dongshuang Wu[e] and Tong Li*[a]

Received 30th May 2025, Accepted 25th July 2025
DOI: 10.1039/d5fd00092k

Developing active and stable bifunctional electrocatalysts for the oxygen reduction reaction (ORR) and oxygen evolution reaction (OER) is essential for a wide range of applications of rechargeable air batteries, water electrolysers, and fuel cells. Here, we report that single-phase face-centred cubic structured PtPdFeCoNi high-entropy alloy (HEA) nanoparticles, synthesized *via* a facile colloidal synthesis approach, possess a good combination of activity and stability toward OER and ORR. Specifically, pristine PtPdFeCoNi HEA nanoparticles exhibit an overpotential of 306 mV at 10 mA cm^{-2} for OER and a half-wave potential of 0.82 V *versus* RHE for ORR, with a narrow overvoltage (ΔE) of 0.71 V in alkaline media, outperforming commercial Pt/C and RuO_2 benchmark electrocatalysts. The OER and ORR activity of the HEA nanoparticles do not change significantly after prolonged electrochemical cycling (3000 cycles). Using X-ray photoelectron spectroscopy and transmission electron microscopy, we found no evident structural, morphological and compositional changes on the HEA nanoparticle surfaces after ORR cycling, explaining its high activity and stability. In contrast, after extended OER cycling, the PtPdFeCoNi nanoparticle surfaces transform into an amorphous layer embedded with Fe-, Co-, and Ni-rich oxyhydroxides, as well as Co-rich oxides, which likely promote activity. Additionally, the shell oxyhydroxide and oxide layer could prevent the continuous dissolution of Pt and Pd, providing long-term

[a]*Faculty of Mechanical Engineering, Atomic-scale Characterisation, Ruhr-Universität Bochum, Universitätsstraße 150, 44801 Bochum, Germany. E-mail: priya.jain@rub.de; tong.li@rub.de*
[b]*Zentrum für Grenzflächendominierte Höchstleistungswerkstoffe (ZGH), Ruhr-Universität Bochum, Universitätsstraße 150, 44801 Bochum, Germany*
[c]*Department of Heterogeneous Catalysis, Max-Planck-Institut für Kohlenforschung, Kaiser-Wilhelm-Platz 1, 45470 Mülheim an der Ruhr, Germany*
[d]*Laboratory of Industrial Chemistry, Ruhr University Bochum, 44780 Bochum, Germany*
[e]*School of Materials Science and Engineering, Nanyang Technological University, Singapore 639798, Singapore*
[f]*Catalysis and Energy Materials Group, IMDEA Materials Institute, Calle Eric Kandel 2, 28906, Getafe, Madrid, Spain*

stability. Overall, this work underscores the importance of correlating morphological, structural, and compositional changes of HEA nanocatalysts with electrocatalytic performance, for understanding how individual elements behave toward bifunctional oxygen electrocatalysis.

1 Introduction

Developing efficient bifunctional oxygen electrocatalysts is necessary for advancing reversible energy storage and conversion systems such as metal–air batteries and regenerative fuel cells.[1–4] However, designing electrocatalysts that excel at both the oxygen evolution reaction (OER) and the oxygen reduction reaction (ORR) remains challenging due to their different operating conditions and mechanistic demands.[2,5] RuO_2 and Pt/C are the benchmark electrocatalysts, but they suffer from limited bifunctionality, high cost, and poor long-term stability, particularly in alkaline environments.[6,7] One strategy to mitigate these challenges is synthesizing alloy nanostructures. Binary and ternary alloy nanostructures, especially those combining noble metals (*e.g.*, Pt, Pd) with 3d transition metals (*e.g.*, Fe, Co, Ni), can improve catalytic activity through d-band tuning, reduce noble metal usage, and lower costs.[8–10] To further reduce the amount of noble metal usage and enhance the bifunctional electrocatalytic performance, high-entropy alloy (HEA) nanoparticles offer a vast compositional space and exciting opportunities to search for new generations of bifunctional oxygen electrocatalysts.[11–13]

HEAs are multicomponent alloys composed of five or more principal elements in equimolar ratios with high configurational entropy (>1.5R), which is thought to stabilize single-phase solid solutions.[14–16] The inherent compositional complexity and structural distortion in HEAs are found to break conventional linear scaling relationships, offering multiple atomic, geometric, and electronic configurations that can significantly improve the adsorption energies of reaction intermediates.[17] For instance, face-centred cubic (fcc) FeCoNiMoW HEAs demonstrated an efficient bifunctional oxygen electrocatalysis with a low overvoltage (ΔE), *i.e.* 0.75 V, between the OER potential at 10 mA cm^{-2} and the ORR half-wave potential.[18] Also, adding Pd into FeCoNiCu alloys was found to enhance OER activity since Pd addition diminishes the energy barrier associated with the rate-determining step (RDS) toward OER.[19] The improved electrocatalytic performance is often attributed to the high configurational entropy, lattice distortion, and sluggish diffusion inherent in HEAs, which contribute to their structural stability and catalytic efficiency.[20,21] However, it remains elusive as to why and how the entropy effect enhances the reaction kinetics due to a poor understanding of the nature of the active regions. Additionally, these active regions evolve, reconstruct, and transform during the electrocatalytic reactions. For example, our recent studies have shown that the electrocatalyst surfaces transform into (oxy)hydroxides under OER conditions.[22,23] Additionally, alloy-based electrocatalysts suffer from metal dissolution, which compromises their structural integrity and long-term stability. Cherevko and coworkers demonstrated that Pt/IrO_2 experienced significant metal loss when subjected to alternating ORR and OER cycles, ultimately limiting its operational lifetime.[22] Further studies on PtNi and PtCo alloys also indicated the high ORR activity due to optimised surface electronic structures, but they lack

stability due to metal leaching and structural degradation during electrochemical cycling.[23,24]

Essentially, most metal components transform into soluble species at high pH (13–14) and under OER and ORR operating conditions, as indicated by Pourbaix diagrams, leading to leaching and eventual degradation of the electrocatalysts.[25] For HEA electrocatalysts, the severe lattice distortion induced by the atom size differences and associated lattice strain was speculated to lower the dissolution rates during the electrocatalytic reaction, thereby enhancing stability. However, few works focused on investigating the morphological, structural, and compositional changes of electrocatalyst surfaces after the reactions.[12,26,27] Therefore, this study aims to establish the structure–performance correlations before and after electrocatalytic reactions to better understand the mechanisms responsible for the enhanced activity and stability of the HEA electrocatalysts. Herein, we combined X-ray photoemission spectroscopy (XPS), transmission electron microscopy (TEM) and *in situ* Raman spectroscopy with electrochemical measurements, to investigate the surface changes of PtPdFeCoNi HEA nanoparticles under the OER and ORR conditions, respectively. PtPdFeCoNi was selected since Pt and Pd[7,9,28] are expected to offer high ORR activity and Ni, Co, Fe are most likely active for OER.[29] We demonstrate that the PtPdFeCoNi HEA nanoparticles maintain structural integrity and compositional uniformity after extended ORR cycling conditions without detectable morphological or phase alterations. However, under OER conditions, a dynamic and selective surface transformation occurs, which enhances the activity and stability.

2 Results and discussion

2.1 Preliminary structural characterization

The PtPdFeCoNi HEA nanoparticles were synthesized *via* a facile one pot colloidal method under inert conditions, using oleylamine (OAm) as the solvent and ascorbic acid as the reducing agent.[30] The synthesis was carried out at a temperature of 280 °C to ensure simultaneous reduction and effective alloying of the metal precursors (Fig. 1a). Powder X-ray diffraction (PXRD) patterns of the as-synthesized nanoparticles display broad diffraction peaks characteristic of a single fcc phase, with the reflections indexed to the (111), (200), and (220) planes located at approximately 40.8°, 47.3°, and 69.2°, respectively (Fig. 1b).[31] These peaks exhibit a clear shift towards higher angles compared to pure Pt (JCPDS No. 04-0802), indicative of lattice contraction due to the incorporation of smaller-sized atoms (*i.e.*, Fe, Co, and Ni) and associated compressive strain in the alloyed structure. Selected area electron diffraction (SAED) patterns, recorded from a few tens of nanoparticles, also show concentric rings matching the fcc phase (Fig. 1c). The TEM image, in Fig. 1d, shows that the nanoparticles possess a near-spherical morphology with a narrow size distribution and an average particle diameter of 8 ± 2 nm (Fig. 1d and e). The high monodispersity suggests controlled nucleation and growth during synthesis. High-resolution transmission electron microscopy (HR-TEM) revealed well-defined lattice fringes with a measured *d*-spacing of 0.235 nm, corresponding to the (111) plane of the fcc lattice (Fig. 1f). The 1–2 nm surface layer with reduced contrast may arise from the carbonaceous residues or organic ligands. The synthesis was repeated three times with consistent results of single fcc phase with similar nanoparticle size.

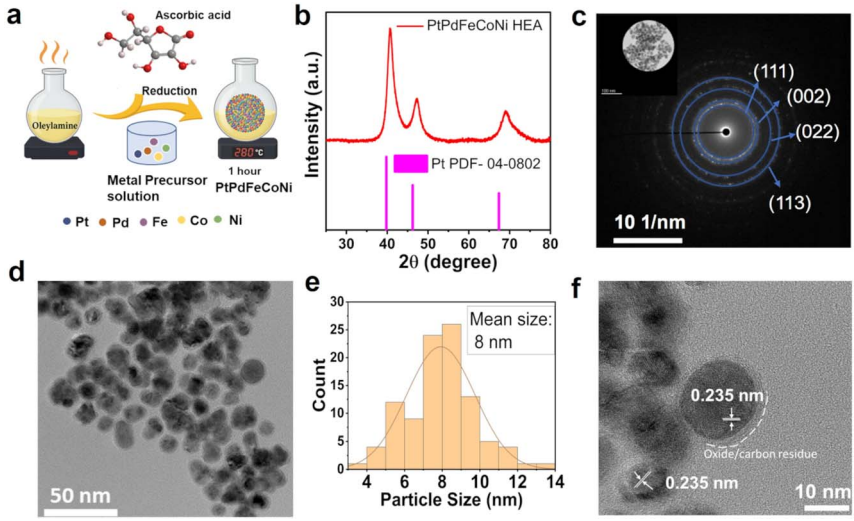

Fig. 1 (a) Schematic illustration of the synthesis process for PtPdFeCoNi HEA nanoparticles using a colloidal method with oleylamine and ascorbic acid (a reducing agent) at 280 °C for 1 h, (b) powder X-ray diffraction (PXRD) pattern of the synthesized PtPdFeCoNi HEA nanoparticles, showing the fcc phase with the Pt standard pattern (PDF# 04-0802). (c) Selected area electron diffraction (SAED) pattern with diffraction rings indexed to the (111), (002), (022), and (113) planes of an fcc structure, (d) transmission electron microscopy (TEM) image of the PtPdFeCoNi nanoparticles. (e) Histogram of the particle size distribution obtained from TEM images, showing an average particle size of ~8 nm. (f) High-resolution TEM (HR-TEM) image of individual PtPdFeCoNi nanoparticles with lattice fringes with an interplanar spacing of 0.235 nm corresponding to the (111) planes of the fcc lattice.

To further assess the elemental distribution, TEM/energy-dispersive X-ray spectroscopy (EDS) was employed. The EDS mappings, shown later in Fig. 5, reveal an even distribution of Pt, Pd, Fe, Co, and Ni across the nanoparticles, with an average composition of ~16 at% Pt, ~15 at% Pd, ~20 at% Fe, ~28 at% Co and 21 at% Ni (Table 1) indicating that the five elements were fully alloyed. The calculated configurational entropy (ΔS_{config}) of the alloy system, using the equation $\Delta S_{\text{config}} = -R\sum x_i \ln x_i$ (where R is the gas constant and x_i is the mole fraction of each element), was found to be $1.57R$ J mol^{-1} K^{-1}, slightly exceeding the

Table 1 The surface atomic % of different metals on the surface of PtPdFeCoNi HEA calculated using XPS and EDX. XPS quantification was based on Ni, Fe, and Co 3p, Pt 4f, and Pd 3d core levels using Al Kα excitation

	Pristine (at%)		Post OER (at%)		Post ORR (at%)	
Metal	XPS	EDX	XPS	EDX	XPS	EDX
Pt	27.2	16.0	7.2	16.5 ± 9.7	23.5	17.3
Pd	11.1	14.9	3.3	18.1 ± 10.1	10.2	16.9
Fe	18.9	20.1	14.4	21.7 ± 8.4	21.6	20.1
Co	25.2	27.7	57.2	21.9 ± 12.2	26.4	26.6
Ni	17.5	21.2	17.7	21.5 ± 9.3	21.6	19.0

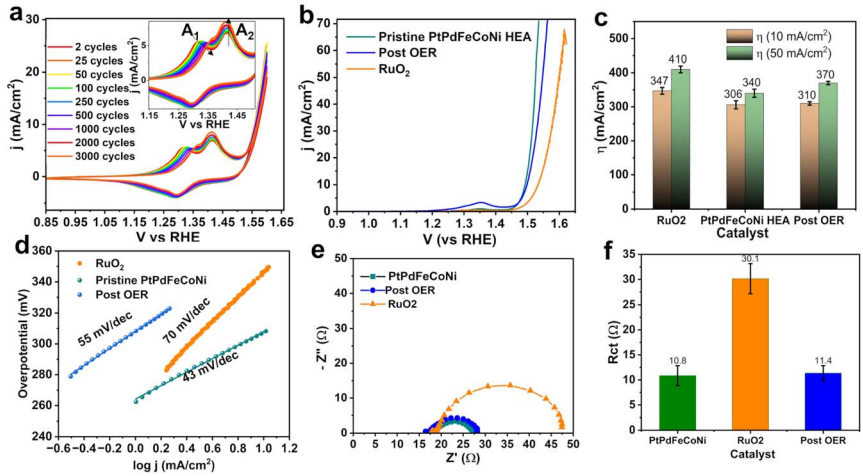

Fig. 2 (a) Cyclic voltammetry (CV) scans of the PtPdFeCoNi HEA catalyst in 1 M KOH over 3000 cycles at a scan rate of 50 mV s^{-1}, (inset: redox peaks in the potential region of 1.15–1.45 V *vs.* RHE), (b) linear sweep voltammetry (LSV) curves at 10 mV s^{-1} comparing the pristine PtPdFeCoNi HEA, post-3000 CV cycles, and benchmark RuO_2 catalyst. (c) Bar chart comparing the overpotentials required to achieve current densities of 10 and 50 mA cm^{-2}, (d) Tafel plots derived from the LSV data for PtPdFeCoNi, post-CV cycles, and RuO_2 (e) Nyquist plots from electrochemical impedance spectroscopy (EIS) measurements at 1.50 V *vs.* RHE. (f) Comparison of R_{ct} values extracted from Nyquist plots for PtPdFeCoNi, RuO_2 and Post CV cycle samples.

threshold of 1.5*R*, characteristic of HEAs,[18] although the five elements do not have an equal composition. In brief, our facile approach can consistently yield nano-sized (~8 nm) single-fcc-phase PtPdFeCoNi HEA nanoparticles.

2.2 Electrochemical activity and stability

To evaluate the bifunctional oxygen electrocatalytic performance of the PtPdFeCoNi HEA nanoparticles, we performed linear sweep voltammetry (LSV) and cyclic voltammetry (CV) under the OER and ORR conditions, respectively. Firstly, we focused on the activity and its changes toward OER. CV measurements were carried out in semiconductor grade 1.0 M KOH using a rotating disc electrode (RDE) at 50 mV s^{-1} at 1600 rpm under the OER conditions (Fig. 2a). LSV of the pristine and 3000-cycle (termed post-OER) samples were performed at 10 mV s^{-1} to compare the activity changes (Fig. 2b). The electrochemical measurements were repeated three times under the same conditions to ensure consistency. All electrochemical data were normalized to the geometric surface area of the electrode (0.124 cm^2), and 95% *iR* compensation was applied to ensure accuracy. The LSV plot, shown in Fig. 2b, demonstrates that the pristine PtPdFeCoNi HEA nanoparticles have an overpotential of 306 mV at 10 mA cm^{-2}, outperforming RuO_2, which exhibits a higher overpotential of 340 mV. Even after undergoing 3000 CV cycles, the activity of post-OER HEA nanoparticles does not change, maintaining a low overpotential of 310 mV (Fig. 2b). This performance is further summarized in Fig. 2c, which compares the overpotentials of pristine and post-OER PtPdFeCoNi and RuO_2 catalysts needed to reach both 10 and 50 mA cm^{-2}.

The PtPdFeCoNi HEA nanoparticles consistently exhibit lower overpotential values than RuO_2 at both current densities, suggesting the high activity of HEA nanoparticles as well as their resilience under prolonged OER cycling operation.

Notably, the CV curves in Fig. 2a reveal the gradual emergence and intensification of distinct redox peaks located at ~1.25 V (A_1) and ~1.40 V (A_2) *vs.* RHE (inset, Fig. 2a). These features are attributed to the Co^{2+}/Co^{3+} and Ni^{2+}/Ni^{3+} redox transitions, respectively.[32–35] Throughout cycling, these peaks shift anodically and increase in intensity, indicating progressive surface oxidation and reconstruction. Rather than degrading the catalyst, this behaviour possibly signifies a dynamic surface reconstruction and transformation process in which the Ni and Co atoms within the HEA matrix convert into catalytically active phases since the OER activity is maintained with nearly no changes (Fig. 2b). Remarkably, despite this surface transformation, the OER current density remains stable, highlighting the excellent electrochemical robustness of the PtPdFeCoNi HEA nanoparticles.

Additionally, we derived the Tafel slopes from the LSV curves, Fig. 2d. The pristine PtPdFeCoNi displays a Tafel slope of 44 mV dec^{-1}, significantly lower than that of RuO_2 (71 mV dec^{-1}), suggesting more favourable reaction kinetics and a faster OER pathway facilitated by the multimetallic composition. After 3000 CV cycles, the Tafel slope of the HEA nanoparticles increases slightly to 56 mV dec^{-1}, which still represents kinetically superior behaviour relative to RuO_2. This improvement in kinetic parameters can be attributed to the surface activation observed during CV cycling, wherein electrochemically inert surface atoms are gradually transformed into active catalytic sites. Electrochemical impedance spectroscopy (EIS) was also employed to probe the interfacial charge transfer properties at 1.50 V *vs.* RHE. The Nyquist plots in Fig. 2e show that the pristine HEA has a notably smaller semicircle diameter compared to RuO_2, corresponding to a lower charge transfer resistance (R_{ct}). Quantified in Fig. 2f, the pristine PtPdFeCoNi HEA exhibits an R_{ct} of 10.1 Ω, which only increases marginally to 11.3 Ω after 3000 CV cycles, further confirming the minimal degradation of the catalyst's electronic interface. In contrast, RuO_2 presents a substantially higher R_{ct} of 30.1 Ω, revealing its inferior charge transport characteristics.

Further insight into surface dynamics was gained from electrochemical surface area (ECSA) measurements derived from double-layer capacitance (C_{dl}) values (Fig. S1). Interestingly, the ECSA of the PtPdFeCoNi HEA nanoparticles increases from 2.4 cm^{-2} in its pristine state to 6.8 cm^{-2} after 3000 CV cycles, consistent with the ongoing surface reconstruction process inferred from the redox peak evolution in CV. This observation reinforces the hypothesis that electrochemical cycling activates additional catalytic sites or new surface species. In addition to CV cycling, long-term stability assessments *via* chronopotentiometry at 10 mA cm^{-2} was performed (Fig. S2a). The PtPdFeCoNi HEA nanoparticles could sustain OER conditions for over 80 h with only ~50 mV potential drift. These results affirm that PtPdFeCoNi HEA exhibit not only enhanced OER activity but can also withstand harsh oxidative environments.

The ORR performance of the synthesized PtPdFeCoNi HEA nanoparticles was systematically evaluated in O_2-saturated 0.1 M KOH electrolyte using rotating RDE (RRDE) and benchmarked against commercial 20 wt% Pt/C under identical conditions. CV measurements were performed in both N_2- and O_2-saturated electrolytes to probe the electrochemical behaviour and onset of the ORR activity. Fig. 3a shows that the PtPdFeCoNi HEA nanocatalyst exhibits an onset potential

(E_{onset}) of 0.96 V and a half-wave potential ($E_{1/2}$) of 0.82 V. While being slightly lower than that of commercial Pt/C ($E_{1/2}$ = 0.90 V), the HEA still demonstrates a high intrinsic ORR activity, especially considering its lower Pt content compared to commercial Pt/C. To further evaluate the ORR activity in a mass-transport-limited regime, LSV measurements, shown in Fig. 3b, reveal that the PtPdFeCoNi HEA nanoparticles reach a diffusion-limited current density (j_d) of ~6 mA cm^{-2} at 0.20 V *vs.* RHE, closely matching the performance of Pt/C (j_d ~7 mA cm^{-2}). After 3000 CV cycles (Fig. 3b (inset)) between 1.00 V and 0.45 V *vs.* RHE, the $E_{1/2}$ exhibits a negligible shift (from 0.82 V to 0.80 V), and the loss in the current density at 0.82 V *vs.* RHE was only ~9%, indicating the high stability of the as-synthesized PtPdFeCoNi HEA nanoparticles. Additionally, the Tafel slope for the pristine PtPdFeCoNi HEA nanoparticles was calculated to be 79 mV dec^{-1} (Fig. 3c), only slightly higher than the benchmark Pt/C catalyst (63 mV dec^{-1}). After 3000 CV cycles, the Tafel slope of PtPdFeCoNi HEA nanoparticles increases marginally to 80 mV dec^{-1}, suggesting negligible degradation in kinetic performance. This indicates efficient charge transfer processes and minimal deterioration of active sites, even under prolonged electrochemical cycling conditions.

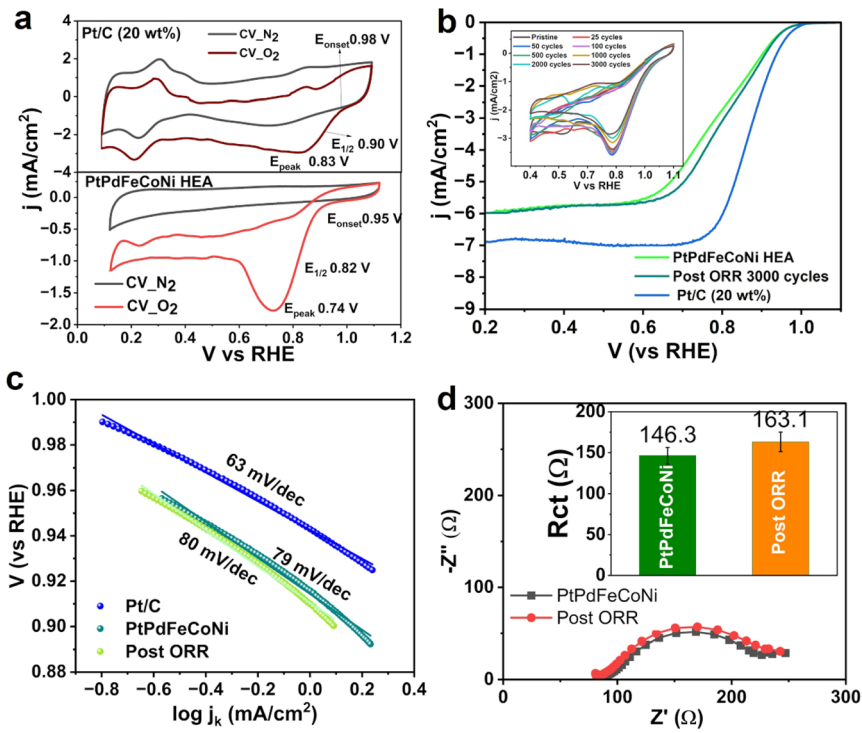

Fig. 3 (a) Cyclic voltammetry (CV) curves recorded at 50 mV s^{-1} in N_2- and O_2-saturated 0.1 M KOH solution for PtPdFeCoNi HEA and commercial Pt/C (20 wt%), (b) linear sweep voltammetry (LSV) at 10 mV s^{-1} and 1600 rpm in O_2-saturated 0.1 M KOH showing the ORR performance of pristine PtPdFeCoNi HEA, post-3000 cycle sample, and Pt/C, inset: 3000 CV cycles in O_2 saturated 0.1 M KOH for PtPdFeCoNi HEA sample. (c) Tafel slopes calculated from LSV curves for pristine and post-CV cycle PtPdFeCoNi HEA and Pt/C, (d) Nyquist plots from electrochemical impedance spectroscopy (EIS) in O_2-saturated 0.1 M KOH. Inset: bar chart comparing R_{ct} values of pristine and post-ORR HEA catalyst.

To understand the interfacial charge transport behaviour, EIS was conducted at 0.82 V *vs.* RHE. The Nyquist plots in Fig. 3d revealed a small semicircle for the pristine HEA, corresponding to a charge transfer resistance (R_{ct}) of 146.3 Ω. After 3000 CV cycles, R_{ct} slightly increased to 163.1 Ω, which suggests that the electrode–electrolyte interface remains largely intact. This minor rise in R_{ct} is consistent with the minimal losses in both current density and onset/half-wave potential, confirming that the ORR activity of PtPdFeCoNi HEA nanocatalysts remains unchanged after extended CV cycling.

Further mechanistic insights were derived from the Koutecky–Levich (K–L) plots obtained by varying rotation rates from 400 to 2500 rpm. The K–L plots in Fig. S2b display good linearity, confirming first-order kinetics with respect to dissolved oxygen concentration. Using the K–L equation, the kinetic current density (j_k) at 0.82 V (*vs.* RHE) was calculated to be 3.5 mA cm^{-2}. Additionally, RRDE analysis applying a constant potential to oxidize H_2O_2 at the ring, yielded an electron transfer number (n) of approximately 3.98 (Fig. S2c), indicating a highly selective four-electron ORR pathway with negligible peroxide formation. This behaviour reflects a nearly ideal reduction of O_2 to H_2O, demonstrating the PtPdFeCoNi HEA's capability to suppress side reactions (*i.e.* the formation of H_2O_2) and maximize efficiency. Such remarkable activity of the PtPdFeCoNi HEA nanoparticles can be attributed to the synergy between its noble and 3d transition metal constituents. Pt and Pd are well-known for their optimal binding energies with oxygenated intermediates, facilitating O_2 activation and reduction.[7,9,28] Meanwhile, Fe, Co, and Ni are likely modulating the electronic structure of the surface, tuning the d-band center and improving adsorption/desorption energetics for ORR intermediates.[36] This interplay likely enhances both the activity and stability of the catalyst, aided further by the high configurational entropy that resists agglomeration and surface deactivation. The chronopotentiometry measurements at a constant current density of 3 mA cm^{-2}, in Fig. S2d, show a constant potential for 24 h, indicating the high stability of the HEA nanoparticles toward ORR. These findings collectively support the hypothesis that the PtPdFeCoNi HEA nanocatalysts suppress surface passivation under the ORR conditions, likely due to the high-entropy stabilization and favourable redox flexibility of surface atoms, particularly Pt and Pd, which retain ORR activity even after extensive cycling.

Given the remarkable electrocatalytic performances of the PtPdFeCoNi HEA nanoparticles toward ORR and OER, its bifunctional capability was further assessed using the oxygen electrode activity descriptor, $\Delta E = E_{10} - E_{1/2}$. The calculated ΔE for the PtPdFeCoNi HEA nanoparticles was 0.71 V, which is slightly lower than that of the commercial Pt/C–RuO_2 benchmark (0.74 V), signifying superior bifunctional electrocatalytic activity (Fig. S3). This reduced potential gap reflects the PtPdFeCoNi HEA nanoparticles' ability to facilitate both OER and ORR with minimal energy loss. Notably, the ΔE value for the HEA nanoparticles is also comparable with reported bifunctional catalysts in recent literature.[18,37–45] as shown in Table S1.

2.3 Structural and compositional changes post OER and ORR

To elucidate the mechanisms for the activation of PtPdFeCoNi HEA nanocatalysts during OER and its high ORR stability, we employed XPS and TEM to reveal the changes in the oxidation state, morphology, structure and composition during

ORR and OER. Firstly, XPS spectra were collected on pristine and after 3000 CV cycles of ORR and OER (Fig. 4a–r). To resolve the quantitative compositional details, the 3p core-level regions of Fe, Co, and Ni were selected for quantification (Fig. S4), since XPS 2p spectra of 3d transition metals (Fe, Co, Ni) exhibit complex multiplet splitting and satellite structures. Using the 3p spectra helps avoid interference from overlapping features, such as the Fe 2p and Ni LMM Auger signals when using an Al Kα source. Additionally, the binding energies of the Fe, Co, and Ni 3p peaks are relatively close (52–68 eV range), ensuring that the inelastic mean free paths (IMFPs)—and thus the electron escape depths—are comparable across these elements. This uniformity improves the precision and consistency of surface atomic quantification in the multimetallic HEA system. Despite this, the XPS 2p spectra core level of Ni, Co and Fe were present, in Fig. 4, to qualitatively reveal the chemical environment and oxidation state due to their strong signal intensity and chemical sensitivity.

High-resolution XPS spectra in the Pt 4f and Pd 3d regions (Fig. 4a–f) suggest that the pristine alloy (Fig. 4a and d) predominantly contains metallic Pt^0 (70.8 eV, $4f_{7/2}$) and Pd^0 (335.4 eV, $3d_{5/2}$), as indicated by the asymmetric line shapes typically associated with metallic species. No detectable Pt^{2+} or Pd^{2+} contributions are

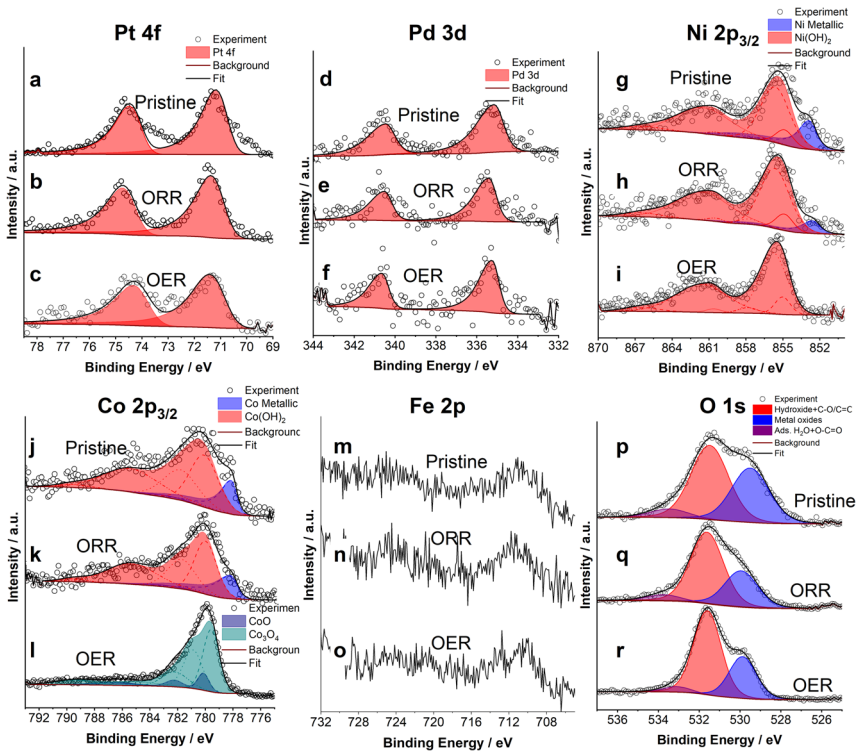

Fig. 4 High-resolution XPS spectra of CoFeNiPdPt HEA nanoparticles in the Pt 4f (a–c), Pd 3d (d–f), Ni $2p_{3/2}$ (g–i), Co $2p_{3/2}$ (j–l), Fe 2p (m–o) and O 1s (p–r) regions for (top) pristine, (center) after 3000 ORR cycles, and (bottom) after 3000 OER cycles. Open circles: experimental data; shaded peaks: deconvoluted components; solid black line: total fit; wine line: background.

observed due to the limitations of the signal-to-noise ratio. After 3000 CV cycles under the ORR conditions (Fig. 4b and e), the spectra remain largely unchanged, implying that Pt and Pd retain their metallic character after extended cycling. The surface composition derived from the XPS spectra of Pt 4f, Pd 3d, and Ni, Co, and Fe 3p, summarised in Table 1, show that the surfaces of the HEA nanoparticles contain ~27 at% Pt and ~11 at% Pd in their pristine state, with similar values after ORR cycling (~24 at% Pt and ~10 at% Pd in the post-ORR samples). This indicates that Pt and Pd act as chemically inert centres within the alloy matrix, resisting degradation during electrocatalysis. Such resistance is characteristic of noble metals and has been proposed to play a stabilizing role in multimetallic systems, serving as supports that maintain the crystalline core and suppress surface amorphization.[46]

As for 3d transition metals, the Ni $2p_{3/2}$ spectrum of the pristine sample (Fig. 4g) is dominated by a broad peak centred around ~855 eV, attributed to Ni^{2+} species in $Ni(OH)_2$, with a smaller contribution at 852.9 eV assignable to metallic Ni^0. Similarly, Co $2p_{3/2}$ spectra of the pristine sample (Fig. 4j) show an envelope consisting of $Co(OH)_2$ as the dominant species (~780 eV), along with a clear Co^0 peak at ~778.3 eV, indicating partial surface oxidation of metallic cobalt. These hydroxide peaks are expected as Ni and Co are easily oxidized to oxide and hydroxide in the ambient environment.[47] After 3000 ORR cycles (Fig. 4h and k), the intensity of the $Ni(OH)_2$- and $Co(OH)_2$-related peak increases, while the metallic Ni^0 and Co^0 signal contribution slightly decreases but remains detectable. Additionally, the Fe 2p spectrum of the pristine sample appears weak and noisy, as it was recorded using a non-monochromated Mg Kα source to avoid spectral overlap with the Ni LMM Auger signals, which interfere with the Fe 2p region around 710–720 eV when using an Al Kα source. However, the use of Mg Kα introduces broader peaks and reduced signal intensity due to its inherently lower spectral resolution compared to a monochromated Al Kα source. Based on our 3p quantification (Table 1), the Co, Ni, and Fe concentrations are ~25 at%, 17 at%, and 19 at%, respectively, in the pristine state and ~26 at%, 22 at%, 22 at% after 3000 ORR cycles. The Ni concentration increase is likely due to the slight decrease in Pt concentration after ORR (Table 1), inferring a slight Pt dissolution during ORR cycling. Despite this, the overall surface composition remains relatively stable during ORR with only minor fluctuations in individual metal concentrations, compared to binary PtNi and PtCo systems,[23,24] where pronounced Ni and Co dissolution occurs.

Similar to Pt and Pd after ORR, both retain their metallic state after 3000 cycles of OER (Fig. 4c and f). However, their surface concentrations decrease significantly to ~7 at% for Pt and ~3 at% for Pd after OER cycling (Table 1). For Ni, the Ni^0 peak diminishes nearly completely (Fig. 4i), and the spectrum is entirely dominated by the $Ni(OH)_2$-related multiplet splitting components, indicating complete conversion of the near-surface Ni into Ni^{2+}. Similarly, the Co^0 peak is no longer visible (Fig. 4l), and the spectrum is deconvoluted into CoO and Co_3O_4 components, indicating progressive oxidation and the formation of stable Co^{2+}/Co^{3+} oxides. Additionally, the Co concentration increases considerably from ~25 at% in the pristine state to ~57 at% after OER cycling, while the Ni content remains constant at ~18 at% before and after OER (see Table 1). The increased Co content likely arises from the formation of a Co-rich surface oxide layer during anodic cycling, as supported by thermodynamic trends in the Pourbaix diagram.[48]

These results imply that the PtPdFeCoNi HEA surfaces transform to (Ni, Co)$(OH)_2$ and Co-based oxide after prolonged OER cycling. In our previous work,[49] Co^{3+} in CoOOH was observed after 100 cycles of OER. Similarly, Ni oxyhydroxide is expected to form before OER, based on the observation of the A_2 peak at 1.40–1.45 V *vs.* RHE corresponding to the Ni^{2+}/Ni^{3+} transition. The existence of Co- and Ni-based hydroxides after OER cycling suggests that the oxyhydroxide formed during anodic sweep is highly reversible, reducing to its hydroxide form upon cathodic sweep. This is further supported by previous findings,[50] indicating that NiOOH, although formed under anodic conditions, is rapidly reduced to $Ni(OH)_2$ once the potential is removed, explaining its absence in *ex situ* XPS.

Additionally, Fe is likely also incorporated in the Ni, Co-based oxyhydroxide, while it is difficult to confirm the oxidation of Fe since its signal after 3000 OER cycles becomes slightly more defined (Fig. 4o), showing a broad feature centred around ~712.8 eV, which may indicate the formation of oxidized Fe species.[51] However, due to the limited signal-to-noise ratio and the absence of distinguishable satellite structures, definitive chemical-state identification is not possible. To investigate changes in Fe, the 3p spectra (Fig. S4) show distinct shifts to higher binding energies, indicating oxidation. Although some noise is present, a consistent trend is observed for Co, Ni, and Fe. In its pristine state, the concentration of Fe is approximately 19 at%, which decreases slightly to approximately 14 at% after 3000 OER cycles (Table 1), likely due to Fe leaching.

To further examine the oxygen species formed on the surfaces of PtPdFeCoNi HEA nanocatalysts after ORR and OER cycling, we performed detailed O 1s spectra analysis, Fig. 4p–r. Deconvolution of the O 1s spectra reveals three main components: a low-binding-energy peak at ~530.0 eV assigned to lattice oxygen (O^{2-}) in metal oxides, a mid-binding-energy peak at ~532.3 eV attributed primarily to surface hydroxyls (OH^-) and potentially overlapping C–O/C=O species, and a high-binding-energy shoulder near ~533.9 eV associated with adsorbed H_2O or O–C=O species. In the pristine sample (Fig. 4p), both components from the lattice O^{2-} component and surface hydroxyls (OH^-) are present, further confirming the presence of Ni, Co-based hydroxide and oxide species that possibly arise from Fe due to its low heat of oxide formation.[52] Following 3000 ORR cycles (Fig. 4q), the lattice O^{2-} component decreases slightly, suggesting a reduction of the surface oxides but only marginally. In contrast, after 3000 OER cycles (Fig. 4r), the metal oxide contribution decreases to ~32%, accompanied by a >10% rise in the hydroxide-related component (Table S2). This evolution reflects a conversion of lattice-bound oxygen anions into hydroxylated surface phases during OER cycling. The surface of PtPdFeCoNi HEA nanocatalysts is predominantly covered by hydroxide species. Note that the *ex situ* XPS captures the catalyst's resting state after potential removal, during which the electrochemically formed oxyhydroxides are rapidly reduced back to their corresponding hydroxides. As such, the dominant O 1s feature assigned to surface hydroxyls likely represents the catalytically active phase in its resting state, *i.e.*, hydroxide species. In addition, the metal oxide component is also present on the surfaces after OER cycling, likely due to the formation of Co-rich oxides (Fig. 4l).

In summary, the XPS data demonstrate that under ORR conditions, the PtPdFeCoNi HEA surface remains largely unchanged. In contrast, OER cycling induces significant surface reconstruction, characterized by the formation of Ni–Co–Fe (oxy)hydroxide species, which subsequently revert *ex situ* to their resting-

state forms—primarily hydroxides. Additionally, Co-rich oxides are also formed during OER cycling. Throughout both electrochemical processes, Pt and Pd remain in their metallic states, acting as stable, redox-inert scaffolds. While *ex situ* XPS provides a snapshot of thermodynamically stable post-reaction states (resting state), the convergence of surface spectroscopic signatures with electrochemical redox features (A_1 and A_2 observed in Fig. 2a) enables a coherent mechanistic interpretation: anodic oxidation of metal oxides into catalytically active oxyhydroxides, followed by reversion to their reduced forms upon potential removal, which constitutes a reversible redox cycle central to OER activity.

To further interrogate the morphological, compositional and structural changes on the surfaces of PtPdFeCoNi HEA nanoparticles, scanning TEM (STEM)/EDS and HR-TEM were carried out on samples before and after 3000 CV cycles of OER and ORR. Fig. 5a contains the STEM image of pristine PtPdFeCoNi HEA nanoparticles, revealing that the top 1–2 nm of surface might contain more Fe, Co, Ni and less Pt and Pd than the core of the nanoparticles, since the nanoparticle core is brighter than the surface layer, indicating the higher atomic mass in the core from the Z-contrast STEM images. Indeed, the STEM/EDS mapping unveils that the top 1–2 nm of surface is enriched with Fe, Ni and Co (Fig. 5d–f) and Pt and Pd are mainly in the core (Fig. 5b and c) (region within the orange circles). Despite this, all elements are distributed evenly (Fig. 5b–f). Similar elemental distribution and STEM image contrasts were observed for PtPdFeCoNi nanoparticles after 3000 ORR cycles (Fig. 5g–l); this is in line with our XPS data showing that the surfaces nearly do not change during ORR. Additionally, the HR-TEM image in Fig. 6a reveals that the post-ORR nanoparticles retain much of their pristine crystallinity after 3000 CV cycles. HR-TEM images show no significant change in lattice integrity or particle morphology, and SAED patterns remain consistent with the fcc structure (Fig. 6c). No evident surface amorphization or new crystalline phases was observed (Fig. 6a and b), indicating minimal structural transformation under ORR conditions.

In contrast to ORR, OER induces drastic morphological and compositional changes on the surfaces of PtPdFeCoNi nanoparticles. After 3000 OER cycles, the shape of PtPdFeCoNi nanoparticles becomes irregular, with uneven distribution of all elements (Fig. 5m–r). Although Pt and Pd are mainly in the core (marked by the arrows), they possibly suffer from dissolution from the surfaces of the nanoparticles after OER cycling, since Pt and Pd distribution resembles the skeleton of polyhedral nanoparticles (Fig. 5n and o). In addition, Fe, Co and Ni are distributed non-uniformly, wherein some surface regions are enriched with Co (marked by arrows), some with Fe and Ni (Fig. 5p–r). This was further supported by point analysis from STEM-EDX quantification across multiple surface regions (SI Fig. S5 and S6), confirming the compositional inhomogeneity across the nanoparticle surfaces.

Additionally, the top 1–2 nm surfaces of post-OER PtPdFeCoNi nanoparticles become highly structurally disordered and nearly amorphous, as highlighted in Fig. 6d and e. As compared to the pristine HEA with a fringe width of 0.235 nm, the post-OER sample showed an additional fringe width at 0.395 nm (Fig. 6d). The lattice fringes near the nanoparticle edges appear in some regions while they are absent in other regions, suggesting partial surface amorphization (see highlighted region in Fig. 6d). This phenomenon has been previously attributed to the formation of electrochemically active oxyhydroxide layers during prolonged OER

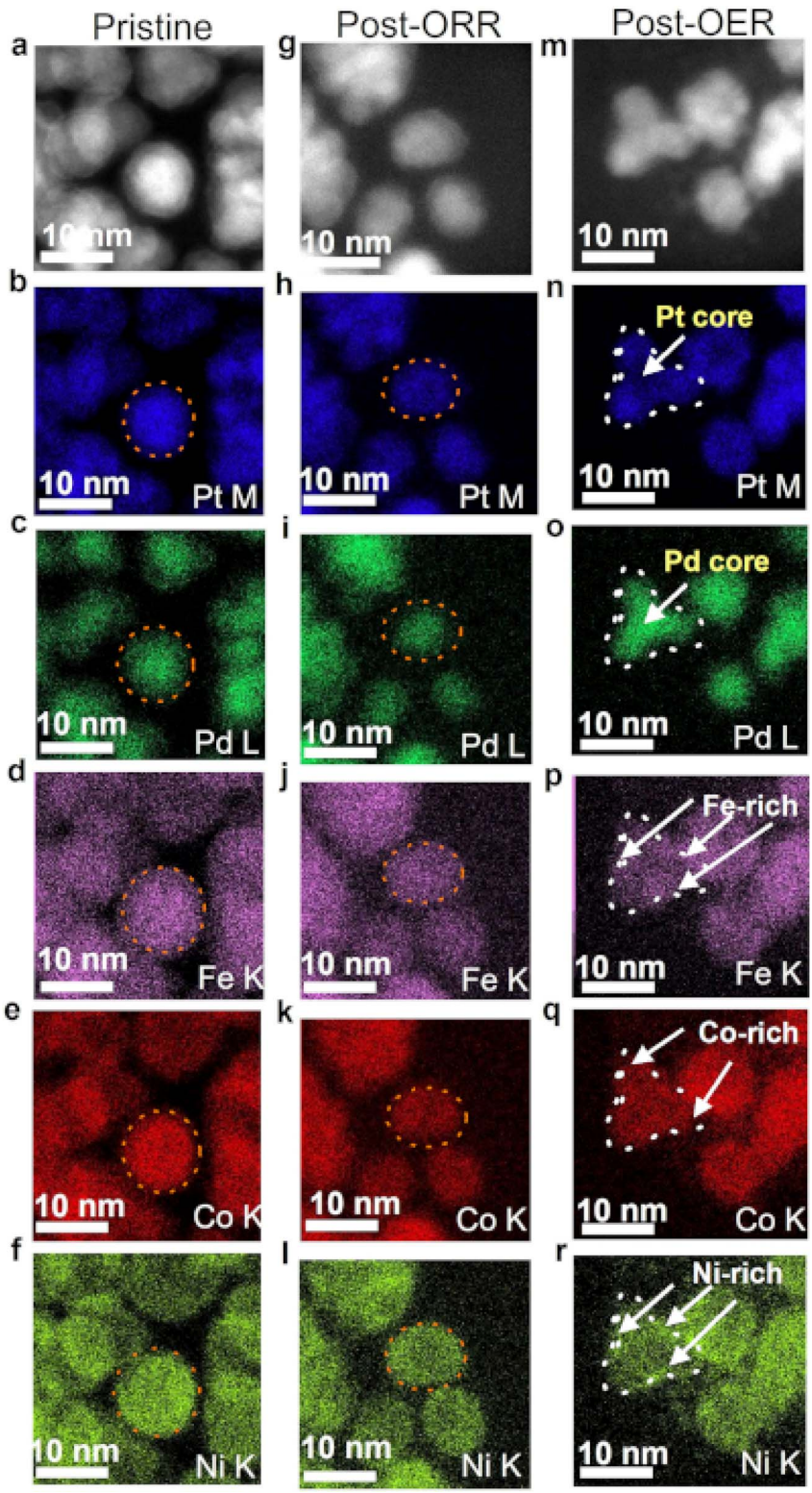

cycling, as reported in spinel- and perovskite oxide nanoparticles toward OER.[53,54] We speculate that similar amorphous (oxy)hydroxides are formed on the surfaces of HEA nanoparticles during OER cycling, as shown by our XPS data that Co-, Ni-, and Fe-rich hydroxides are present on the surfaces after OER cycling. In addition to amorphous (oxy)hydroxides, additional reflections corresponding to Co_3O_4 were observed in the SAED pattern of the post-OER sample (Fig. 6f). The preservation of the fcc reflections alongside the emergence of new Co_3O_4 diffraction features and amorphous (oxy)hydroxide layer suggests the formation of a core–shell-like nanostructure, where the bulk remains crystalline while the surface undergoes reconstruction into electrocatalytically active (oxy)hydroxide and oxide phases. Future work will also include electron energy loss spectroscopy (EELS) mapping to directly probe the oxidation states and better resolve the chemical nature of the surface layers at high spatial resolution. To monitor the leaching of metals, the 0.1 M KOH electrolyte sample was collected after CV cycles from the electrochemical Raman flow cell, and the inductively coupled plasma optical emission spectroscopy (ICP-OES) measurement was carried out (Table S3). There is no significant increase in Co, Fe, Ni, and Pd content in the electrolyte after reaction, denoting the stability of metals in the high-entropy alloy from leaching at harsh electrochemical conditions. The increase in Pt content after the reactions, followed by the leaching of other metals, could originate from the dissolution of the Pt counter electrode.

In addition, *in situ* Raman spectroscopy was performed to investigate the surface species at different potentials under the OER conditions (Fig. S7). A broad band at 400–600 cm^{-1} evolved from the first anodic scan and seems to be stable up to the 1000th CV (Fig. S6b–d). These bands are due to the formation of different (oxy)hydroxide phases, under OER conditions, consistent with the XPS and HR-TEM results. However, a high amount of carbon-containing residuals is present in the nanoparticles, making them challenging to analyse by Raman spectroscopy since the carbon signal at 1300 cm^{-1} and 1600 cm^{-1} (due to D and G bands) is so significant that other intermediate species suffer from a low signal-to-noise ratio (Fig. S6a). A few trials trying to remove the carbon residual were attempted but were not successful. In future studies, efforts will be made to remove organic residuals during nanoparticle synthesis, which may potentially improve the signal-to-noise ratio for XPS and Raman spectroscopy measurements. Additionally, atom probe tomography (APT) will be employed to resolve the compositional evolution of HEA nanoparticle surfaces before and after OER and ORR, respectively. We have attempted APT measurements, but the high carbon residuals in the nanocatalysts make it challenging to prepare APT specimens and find regions with HEA nanoparticles. Methods of removing the carbon residuals will improve the success rate of specimen preparation and APT measurements. Additionally, advanced *in situ* techniques such as XRD and electrochemical TEM would be highly valuable in further confirming the nature,

Fig. 5 STEM EDS elemental maps of Pt M (b, h and n), Pd L (c, i and o), Fe K (d, j and p), Co K (e, k and q), and Ni K (f, l and r) for: (a–f) pristine PtPdFeCoNi HEA, demonstrating a homogeneous distribution of all five elements with Ni, Co, Fe enriched surfaces due to surface oxidation (marked by orange circles); (g–l) post ORR sample indicating minimal changes and; (m–r) post OER showing Pt, Pd in the core with ~1 nm surface layer of Fe, Co, Ni oxides/oxyhydroxides (marked by arrows).

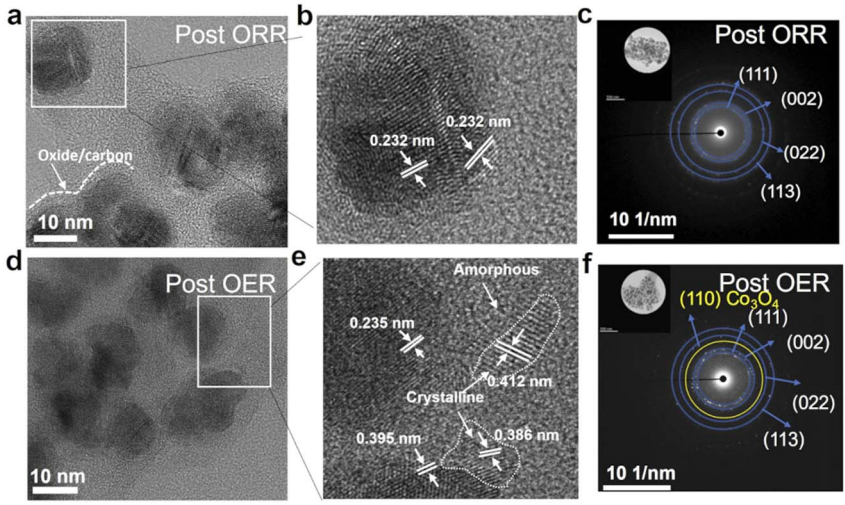

Fig. 6 (a) HR-TEM image of PtPdFeCoNi HEA nanoparticles after 3000 CV cycles under ORR conditions in O_2-saturated 0.1 M KOH, (b) magnified view of the boxed region in (a), showing interplanar spacing of 0.232 nm corresponding to the (111) planes of the fcc structure. (c) SAED pattern post ORR. (d) HR-TEM image of PtPdFeCoNi HEA nanoparticles after 3000 CV cycles under OER conditions in 1 M KOH, (e) magnified view of the boxed region in (d), showing multiple interplanar spacings of 0.235 nm (likely fcc (111) planes), and larger spacings of 0.386 nm and 0.395 nm, possibly indicating partial surface oxidation or formation of oxide phases, (f) SAED pattern after ORR cycles.

dynamics, and reversibility of the structural changes associated with the formation of Ni–Co-based oxyhydroxides and Co_3O_4-type oxide phases. Efforts to combine *ex situ* and *in situ* characterisation methods are underway to reveal the surface transformation of the HEA nanoparticles during the reaction.

In summary, we demonstrate that PtPdFeCoNi HEA nanoparticles exhibit enhanced activity and stability for ORR and OER. Although the pristine PtPdFeCoNi HEA nanoparticles exhibit a single-phase fcc structure (Fig. 1b), top surfaces are slightly oxidised to the Ni- and Co-based hydroxide and likely Fe-containing oxides, based on our XPS data (Fig. 4). Such an oxide/hydroxide layer is extremely thin, most likely 1–2 nm. Which explains their absence in the XRD data due to its detection limit. These results indicate that the surfaces of HEA nanostructured electrocatalysts containing 3d transition metals are inevitably oxidised since Ni-, Co-based hydroxide, and Fe-based oxide are thermodynamically stable in ambient air. This induces a compositional gradient across the surfaces and bulk nanoparticles, where Pt and Pd are more concentrated in the core and Ni, Fe and Co are enriched on the surfaces of the PtPdFeCoNi HEA nanoparticles (as schematically shown in Fig. 7). Notably, Pt and Pd are still present on the surfaces with a content of ~27 at% and 11 at%, respectively, based on our XPS and ICP-OES data (Table 1 and S3). Their presence, along with 3d transition metals, gives rise to the high ORR activity and stability after prolonged CV cycling. Surprisingly, the concentration of all elements on the surface remains unchanged (Table 1), despite significant Ni and Pt dissolution being observed in Pt-based binary electrocatalysts under ORR conditions.[23] These results demonstrate that

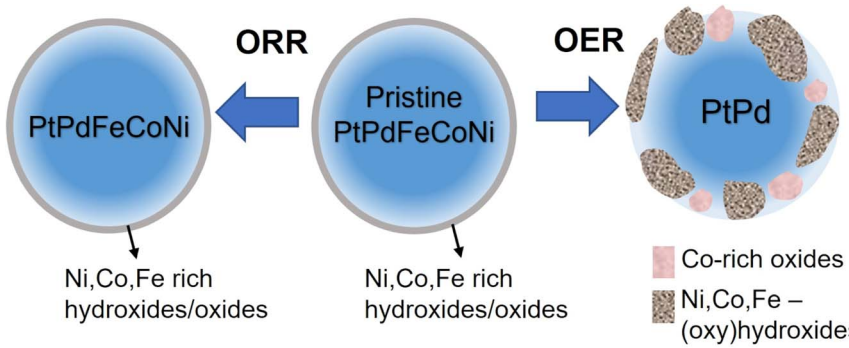

Fig. 7 Schematic representation of surface evolution in PtPdFeCoNi HEA nanoparticles during electrochemical cycling. In the pristine state, the HEA nanoparticle exhibits an homogenous distribution of all five elements, with a stable PtPd-rich core and a uniform surface composed of Fe, Co, and Ni, with some oxides and hydroxides. Post OER electrochemical activation induces surface reconstruction, resulting in the formation of a thin (~1 nm) amorphous shell of transition metal oxides/oxyhydroxides (FeOOH, CoOOH, NiOOH), while the PtPd core remains stable. Post ORR cycling, the PtPd core and Fe, Co and Ni remains stable with a PtPd-rich core and a uniform surface composed of Fe, Co, and Ni, with some oxides and hydroxides.

Pt and Pd, assisted by the presence of 3d transition metals, possess enhanced ORR activity and stability. Similarly, high ORR stability and activity of PtPdFeCoNi HEA nanocatalysts were observed in previous work,[30] where the half-wave potential shifted by only 6 mV after 50 000 cycles of accelerated durability testing. This was attributed to the high configurational entropy, lattice distortion, and sluggish diffusion of the HEAs. In addition to this, we speculate that the presence of a mono- or bilayer of hydroxide and oxide on the surfaces, likely alters the reaction kinetics, which also prevents the dissolution of 3d transition and noble metals, enhancing the ORR activity and stability. Further DFT simulation work is underway to better understand the role of the hydroxide and oxide layer in the activity of PtPdFeCoNi HEA.

For OER, the surfaces of PtPdFeCoNi HEA nanoparticles undergo considerable morphological, composition, and structural changes. The (Ni, Co)-based hydroxide on the pristine PtPdFeCoNi HEA nanoparticle surface most likely transforms to oxyhydroxide during OER,[55,56] as revealed by the A_1 and A_2 peaks that correspond to Co^{2+}/Co^{3+} and Ni^{2+}/Ni^{3+} transitions. Interestingly, such a hydroxide/oxyhydroxide transition is highly reversible as a significant amount of hydroxide is present on the surfaces after 3000 cycles of OER, based on our XPS data (Fig. 4r). The formation of highly reversible oxyhydroxide enhances the OER activity of PtPdFeCoNi HEA nanoparticles since these oxyhydroxides are known to be active towards OER.[57] In addition to hydroxide, Co-based oxide is also formed during OER cycling, likely due to the relatively lower redox potential of Co[58] and thermodynamic stability in alkaline media at our CV potential ranges according to the Co Pourbaix diagram.[48] Notably, Co-based spinels are highly active for OER.[58] The selective formation of Co-rich oxide and Ni, Co, Fe-based hydroxide serves as a passivation layer for segregation and dissolution of 3d transition and noble metals, suppressing their elemental leaching as evident by ICP-OES analysis (Table S3), which preserves the high activity and stability of PtPdFeCoNi HEA

nanoparticles. Thus, the enhanced OER activity and stability are not entirely induced by the high entropy synergistic effect. Instead, the selective formation of (Ni, Co, Fe)-rich oxyhydroxide and Co-rich oxide promotes the activity and stability of PtPdFeCoNi nanoparticles.

3 Conclusion

Overall, we employed a facile colloidal synthesis method to prepare single-phase fcc PtPdFeCoNi HEA nanoparticles for bifunctional oxygen electrocatalysis. Electrochemical testing demonstrates excellent activity for both ORR and OER in alkaline conditions, with long-term durability significantly surpassing that of conventional benchmarks. Our combined XPS, STEM/EDX, and HR-TEM results show that the pristine PtPdFeCoNi HEA nanoparticles are inevitably oxidized, forming a thin (1–2 nm) layer of Ni- and Co-based hydroxides and Fe oxide. We demonstrate that the hypothesis of 'high-entropy synergistic effect' for the improved activity of HEA electrocatalysts requires verification by detailed and systematic characterization of the HEA surfaces, as 3d-transition-metal-containing HEA nanoparticles are likely covered by a thin hydroxide/oxide layer. After prolonged ORR cycling, nearly no compositional, structural, and morphological changes were observed on PtPdFeCoNi HEA nanoparticle surfaces after ORR. In comparison, OER induces the surface transformation to Ni, Co, Fe-based oxyhydroxides and Co-rich spinel-type oxide. This redox-active shell is responsible for enhanced catalytic kinetics, while Pt and Pd preserve the crystalline core, ensuring electrical conductivity and structural durability. The combination of a stable metallic backbone and a dynamically evolving catalytic surface exemplifies the intrinsic advantage of HEA systems with enhanced activity and stability. This work highlights the potential of multimetallic HEA catalysts in overcoming the traditional trade-off between activity and stability in bifunctional electrocatalysis. More importantly, our study highlights the significance of understanding the morphological, structural, and compositional changes of HEA nanocatalysts during electrocatalytic reactions, which may provide valuable guidance for designing future catalysts that evolve and improve during operation.

4 Experimental

4.1 Chemicals

Platinum acetylacetonate, palladium acetylacetonate, cobalt acetylacetonate, iron acetylacetonate, and nickel acetylacetonate were purchased from Sigma-Aldrich. Olylamine, L-ascorbic acid, and potassium hydroxide pellets, were purchased from Sigma-Aldrich. Commercial Pt/C (20%) and RuO_2 were procured from Sigma Aldrich. All the chemicals were used without any purification process.

4.2 Synthesis of PtPdFeCoNi high-entropy alloy (HEA) nanoparticles

To synthesize the HEA nanoparticles, an equimolar mixture (25 mM each) of metal salts was first dissolved in 2 mL of oleylamine, which had been degassed by heating at 100 °C for 30 min under vacuum. Separately, 100 mg of ascorbic acid was dissolved in 1 mL of oleylamine to form a reducing agent solution. In a typical synthesis, 20 mL of oleylamine was added to a round-bottom flask and heated to

approximately 280 °C under an argon atmosphere with continuous stirring. Once the target temperature was reached, the ascorbic acid solution (1 mL) was injected, followed by the 2 mL metal precursor solution. The reaction was maintained at this temperature for 90 min, after which the mixture was allowed to cool to room temperature naturally. The resulting nanoparticles were separated by centrifugation and washed several times using a hexane/ethanol mixture to remove any impurities. The cleaned product was dried at 60 °C for 12 h to obtain a dry nanoparticle powder. Finally, the dried particles were thermally treated at 200 °C for 10 h to remove residual surface ligands.[30]

4.3 Electrochemical measurements

All the electrochemical tests were carried out in a standard three-electrodes cell with 1.0 M KOH (pH = 14) for OER and O_2-saturated 0.1 M KOH for ORR at a rotation speed of 1600 rpm using a potentiostat (Bio-Logic SP-300). A graphite rod was used as a counter electrode, and a Hg/HgO electrode was the reference electrode. The working electrode was prepared as follows: 4 mg electrocatalyst powder was dispersed in the mixture of 705 μL ultrapure water, 250 μL isopropanol and 45 μL Nafion, and sonicated for 30 min. Before electrochemical measurements, a bare glassy carbon electrode (GCE) with a diameter of 4.0 mm was cleaned with alumina slurry and rinsed ultrasonically with ethanol and water for 20 s, successively. A 10 μL dispersion was subsequently dropped on the GCE and dried at room temperature, obtaining a catalyst loading of 0.204 mg cm^{-2}.

For OER, CV measurements were performed between 0 and 0.73 V (*vs.* Hg/HgO) with a scan rate of 100 mV s^{-1} for 3000 cycles in 1.0 M KOH. Linear sweep voltammetry (LSV) was conducted between 0.00 and 0.86 V (*vs.* Hg/HgO) with a scan rate of 10 mV s^{-1}. Electrochemical impedance spectroscopy (EIS) was performed under OER conditions by applying a sine wave signal with a 10 mV amplitude in the frequency range 100 kHz to 0.1 Hz after equilibrating for 5 s at 0.73 V (*vs.* Hg/HgO). The uncompensated series resistance (R_s) of the electrode setup is ~15 Ω from Nyquist plots shown in Fig. 2d. An ohmic drop (iR_s) correction (95%) was applied to compensate for the decrease in the actual electrode potential when compared to the nominal potential due to current flux in the highly resistive system. All electrochemical tests were repeated three times. The measured potentials were calculated from the potential *vs.* reversible hydrogen potential according to the equation:

$$E_{RHE} = E_{Hg/HgO} + 0.118 + 0.059 \times pH.$$

For ORR, the LSV was recorded in O_2 and N_2 saturated 0.1 M KOH within potential range 0.2 V to −0.8 V *vs.* Hg/HgO at a scan rate of 10 mV s^{-1} at 1600 rpm. The K–L plot was derived by performing hydrodynamic voltammetry at various scan rates *i.e.* 400, 800, 1200, 1600, 2000 and 2500 rpm at 10 mV s^{-1} in O_2 saturated electrolyte. Based on the LSV data, the electron transfer numbers were calculated according to the K–L equation:

$$\frac{1}{J} = \frac{1}{J_l} + \frac{1}{J_k} = \frac{1}{B\omega^{1/2}} + \frac{1}{J_k}$$

$$B = 0.2nFC_o(D_o)^{\frac{2}{3}}\nu^{-\frac{1}{6}}$$

$$J_k = nFKC_O$$

where J, J_k, and J_l are the measured current density, kinetic- and diffusion-limiting current densities, respectively. F is the Faradaic constant, D_O is the diffusion coefficient of O_2 in 0.1 M KOH (1.9×10^{-5} cm^2 s^{-1}), ω is the rotation speed, ν is the kinematic viscosity of the electrolyte (1.0×10^{-2} cm^2 s^{-1}), and C_O is the bulk concentration of O_2 (1.2×10^{-6} mol cm^{-3}).[6]

RRDE measurements were carried out at a rotating speed of 1600 rpm. The H_2O_2 yield (H_2O_2%) and electron transfer numbers (n) were then calculated based on the data, using the following equations[6]

$$H_2O_2\% = 200 \times \frac{I_R/N}{I_D + I_R/N}$$

$$n = 4 \times \frac{I_D}{I_D + I_R/N}$$

where I_D is disk current, I_R is ring current, and N is the collection efficiency of the ring electrode (0.420 in this work).[6] XPS and TEM were taken after various CV cycles between −0.8 and 0.2 *vs.* Hg/HgO at a scan rate of 50 mV s^{-1} with a glassy carbon plate as the working electrode in O_2 saturated 0.1 M KOH (and 0–0.65 V *vs.* Hg/HgO in 1 M KOH for OER). Only nanoparticle powder without carbon black and Nafion was used to prepare the suspension, and the loading area is ≈0.5 cm^2, which needs ≈32 μL of suspension for the drop cast.

For stability analysis, chronopotentiometry (CP) was measured at a constant current density (10 mA cm^{-2}) for 80 h (OER) and 3 mA cm^{-2} for 24 hours (ORR). The electrochemical capacitance was measured by CV between 0.974–1.074 V (*vs.* RHE) at various scan rates of 25 mV s^{-1}, 50 mV s^{-1}, 75 mV s^{-1}, 100 mV s^{-1} and 125 mV s^{-1}. The ECSA was calculated from double layer capacitance from CVs at different scan rates according to the following equation[31]

$$\text{ECSA} = C_{dl}/C_s$$

where C_s is the specific capacitance and the value is 40 μF cm^{-2} in alkaline medium. C_{dl} represents the electrochemical double-layer capacitance.

4.4 Material characterization

X-ray diffraction (XRD) patterns were obtained using a Bruker D8 DISCOVER diffractometer equipped with Cu Kα radiation ($\lambda = 1.5418$ Å), scanned slowly at 0.4° per min over a 2θ range of 10° to 90°, with a step size of 0.01°. For transmission electron microscopy (TEM), samples were prepared by depositing a powder suspension onto a copper TEM grid. TEM and high-resolution-TEM (HR-TEM) images were captured using an aberration-corrected JEOL JEM-2200FS operating at 200 kV, and elemental mapping was performed with an Oxford X-max energy-dispersive X-ray (EDX) detector integrated into the

microscope. The local area analysis was performed by selecting the different regions on the EDX map and measuring the spectra. HR-TEM images were processed using Gatan Digital Micrograph software.

X-ray photoelectron spectra (XPS) were recorded using a ULVAC-Phi Versaprobe II™ system equipped with a monochromatic Al Kα X-ray source (1486.6 eV). The instrument provides a minimum beam size of 100 μm and a spectral resolution of 0.5 eV. The source was operated at 15 kV and 13.2 W under ultra-high vacuum conditions. A flood gun was used to neutralize surface charging. Survey scans were acquired with a pass energy of 117.400 eV, and high-resolution spectra were collected at 11.700 eV, both in fixed transmission mode. To isolate overlapping signals in the Fe 2p region—particularly due to Ni LMM Auger and Fe 2p interference—an Mg Kα X-ray source was employed for selected measurements. While this configuration allowed clearer observation of Fe 2p features, it also resulted in lower spectral resolution compared to Al Kα, leading to peak broadening and limited resolution of the Fe 2p region. All spectra were processed using CasaXPS software (version 2.3.25PR1.0). A standard Shirley background was applied to all regions. Binding energies were calibrated to the C 1s peak, set to 284.5 eV as the glassy carbon substrate was exposed partially. Peak fitting was adapted to the nature of each element. Co $2p_{3/2}$ and Ni $2p_{3/2}$ regions were fitted using symmetric Gaussian–Lorentzian product functions GL(*m*), where *m* denotes the Lorentzian fraction (*e.g.*, GL(30) corresponds to 30% Lorentzian and 70% Gaussian). The O 1s region was modeled using an asymmetric LA(1.53, 243) line shape to account for final-state effects in oxidized species. For metallic components, asymmetric line shapes were applied: Pd 3d was fitted using LA(1.9, 7, 2), and Pt 4f using LA(1.2, 85, 70), which represent characteristic tailing from metallic screening. To analyze surface evolution and chemical state changes in the CoFeNiPdPt system, the fitting strategy followed the approach developed by Biesinger *et al.*[59] Reference peak models were applied for Ni (metallic Ni, NiO, $Ni(OH)_2$, γ-NiOOH, β-NiOOH) and Co (metallic Co, CoO, $Co(OH)_2$, Co_3O_4, CoOOH), with constraints on relative binding energy positions, peak areas, and FWHM, ensuring chemically and physically meaningful deconvolution.

In situ electrochemical Raman measurements were conducted using an Invia Renishaw Raman microscope equipped with a 785 nm laser excitation wavelength, 1200 l mm^{-1} grating, and 50× long focal distance objective lens (Leica). The applied potential and current dependence were controlled with a BioLogic SP200 Potentiostat and the electrochemical measurements were performed at room temperature in a customized *in situ* electrochemical Raman flow cell equipped with a quartz measurement window. A Pt wire and a hydrogen electrode (HydroFlex, Gaskatel) were used as the counter and reference electrodes, respectively. The working electrode was prepared by drop-casting the catalyst ink onto a rough gold substrate. The catalyst ink was prepared by dispersing 1 mg of PtPdFeCoNi powder in 100 μL of DMF and ultrasonicated for 30 min. The gold substrate was roughened based on the procedure described in the literature.[60] 0.1 M KOH electrolyte flow into the electrochemical cell was controlled using a peristaltic pump with a flow rate of 8 mL min^{-1}. The Raman spectra were recorded *in situ* in chronoamperometric (CA) mode, at a gradual potential bias increase from 1.0 V up to 1.5 V *vs.* RHE for OER conditions. The electrolyte reservoir is continuously bubbled with Ar for the OER experiment. Prior to each measurement, the energy shift was calibrated using 520 ± 0.5 cm^{-1} peak of

silicon reference. Twenty consecutive scans at 3 s acquisition time at 3.3 mW laser power were performed to record the spectra under liquid environments. Inductively coupled plasma-optical emission spectrometry (ICP-OES) measurements were carried out using a SPECTROGREEN instrument, and the electrolyte solution was sampled from the as-prepared 0.1 M KOH and the outlet of the electrochemical Raman flow cell after the OER and ORR reaction.

Author contributions

T. L. designed, supervised, and coordinated the project. P. J. synthesized the nanoparticles and performed the electrochemical tests. P. H. performed the XPS measurements and analysis. A. K. performed the TEM measurements and P. J. analyzed the TEM data. P. D. and M. M. provided XRD measurements. E. B. and H. T. performed the *in situ* Raman measurements, D. W. provided suggestions. All authors agreed on the content and conclusion of the paper.

Conflicts of interest

There no conflicts to declare.

Data availability

The authors confirm that the data supporting the findings of this study are available within the article and its SI. Additional raw data are available from the corresponding author upon reasonable request.

Supplementary information is available. See DOI: **https://doi.org/10.1039/d5fd00092k**.

Acknowledgements

PJ and TL are grateful for funding from the Deutsche Forschungsgemeinschaft (DFG, German Research Foundation) – Projektnummer 506711657 – CRC1625 (B02 projects) and SPP 2006 (project number 38873549). TL thanks DFG – Projektnummer 388390466-TRR 247 (B09 and S projects). All authors acknowledge the Zentrum für grenzflächendominierte Höchstleistungswerkstoffe (ZGH) at Ruhr University Bochum for the access of infrastructures (JEOL ARM JEM-ARM 200F). We also thank F. Baum for his support during the ICP-OES measurements.

References

1 Z.-F. Huang, J. Wang, Y. Peng, C.-Y. Jung, A. Fisher and X. Wang, *Adv. Energy Mater.*, 2017, **7**, 1700544.
2 K. Zeng, X. Zheng, C. Li, J. Yan, J.-H. Tian, C. Jin, P. Strasser and R. Yang, *Adv. Funct. Mater.*, 2020, **30**, 2000503.
3 X.-M. Liu, X. Cui, K. Dastafkan, H.-F. Wang, C. Tang, C. Zhao, A. Chen, C. He, M. Han and Q. Zhang, *J. Energy Chem.*, 2021, **53**, 290–302.
4 C.-X. Zhao, J.-N. Liu, J. Wang, D. Ren, B.-Q. Li and Q. Zhang, *Chem. Soc. Rev.*, 2021, **50**, 7745–7778.
5 X. Liu, G. Zhang, L. Wang and H. Fu, *Small*, 2021, **17**, 2006766.

6 P. Jain, S. Jha and P. P. Ingole, *ACS Appl. Energy Mater.*, 2023, **6**, 3278–3290.
7 Z. W. Seh, J. Kibsgaard, C. F. Dickens, I. Chorkendorff, J. K. Nørskov and T. F. Jaramillo, *Science*, 2017, **355**, eaad4998.
8 J. Liu, T. Zhang and G. I. N. Waterhouse, *J. Mater. Chem. A*, 2020, **8**, 23142–23161.
9 J. Greeley, I. E. L. Stephens, A. S. Bondarenko, T. P. Johansson, H. A. Hansen, T. F. Jaramillo, J. Rossmeisl, I. Chorkendorff and J. K. Nørskov, *Nat. Chem.*, 2009, **1**, 552–556.
10 X. Tian, X. Zhao, Y.-Q. Su, L. Wang, H. Wang, D. Dang, B. Chi, H. Liu, E. J. M. Hensen, X. W. Lou and B. Y. Xia, *Science*, 2019, **366**, 850–856.
11 A. B. Haruna, E. U. Onoh and K. I. Ozoemena, *Curr. Opin. Electrochem.*, 2023, **39**, 101264.
12 C. Luan, D. Escalera-López, U. Hagemann, A. Kostka, G. Laplanche, D. Wu, S. Cherevko and T. Li, *ACS Catal.*, 2024, **14**, 12704–12716.
13 T. Löffler, A. Ludwig, J. Rossmeisl and W. Schuhmann, *Angew. Chem., Int. Ed.*, 2021, **60**, 26894–26903.
14 X. Zhang, Y. Liu, X. Zhao, Z. Cheng and X. Mu, *Energy Fuels*, 2024, **38**, 19236–19252.
15 K. Huang, B. Zhang, J. Wu, T. Zhang, D. Peng, X. Cao, Z. Zhang, Z. Li and Y. Huang, *J. Mater. Chem. A*, 2020, **8**, 11938–11947.
16 J. W. Yeh, S. K. Chen, S. J. Lin, J. Y. Gan, T. S. Chin, T. T. Shun, C. H. Tsau and S. Y. Chang, *Adv. Eng. Mater.*, 2004, **6**, 299–303.
17 J. Pérez-Ramírez and N. López, *Nat. Catal.*, 2019, **2**, 971–976.
18 R. He, L. Yang, Y. Zhang, D. Jiang, S. Lee, S. Horta, Z. Liang, X. Lu, A. OstovariMoghaddam, J. Li, M. Ibáñez, Y. Xu, Y. Zhou and A. Cabot, *Adv. Mater.*, 2023, **35**, 2303719.
19 S. Wang, B. Xu, W. Huo, H. Feng, X. Zhou, F. Fang, Z. Xie, J. K. Shang and J. Jiang, *Appl. Catal., B*, 2022, **313**, 121472.
20 T. A. A. Batchelor, J. K. Pedersen, S. H. Winther, I. E. Castelli, K. W. Jacobsen and J. Rossmeisl, *Joule*, 2019, **3**, 834–845.
21 Y. Zhang, D. Wang and S. Wang, *Small*, 2022, **18**, 2104339.
22 G. C. da Silva, K. J. J. Mayrhofer, E. A. Ticianelli and S. Cherevko, *J. Electrochem. Soc.*, 2018, **165**, F1376.
23 C. Cui, L. Gan, M. Heggen, S. Rudi and P. Strasser, *Nat. Mater.*, 2013, **12**, 765–771.
24 S. Koh, M. F. Toney and P. Strasser, *Electrochim. Acta*, 2007, **52**, 2765–2774.
25 B. He, F. Bai, P. Jain and T. Li, *Small*, 2025, **21**, 2411479.
26 K. Huang, J. Xia, Y. Lu, B. Zhang, W. Shi, X. Cao, X. Zhang, L. M. Woods, C. Han, C. Chen, T. Wang, J. Wu and Y. Huang, *Adv. Sci.*, 2023, **10**, 2300094.
27 P. Yang, Z. Jiang, Y. Shi, X. Ren, L. Liang, Q. Shao and K. Zhu, *J. Alloys Compd.*, 2023, **947**, 169699.
28 J. Wu, S. Shan, H. Cronk, F. Chang, H. Kareem, Y. Zhao, J. Luo, V. Petkov and C.-J. Zhong, *J. Phys. Chem. C*, 2017, **121**, 14128–14136.
29 H. Y. Jung, J. H. Park, J. C. Ro and S. J. Suh, *ACS Omega*, 2022, **7**, 45636–45641.
30 Y. Yu, F. Xia, C. Wang, J. Wu, X. Fu, D. Ma, B. Lin, J. Wang, Q. Yue and Y. Kang, *Nano Res.*, 2022, **15**, 7868–7876.
31 M. Xie, Y. Lu, X. Xiao, D. Wu, B. Shao, H. Nian, C. Wu, W. Wang, J. Gu, S. Han, M. Gu and Q. Xu, *Adv. Funct. Mater.*, 2025, **35**, 2414537.

32 T. Li, O. Kasian, S. Cherevko, S. Zhang, S. Geiger, C. Scheu, P. Felfer, D. Raabe, B. Gault and K. J. J. Mayrhofer, *Nat. Catal.*, 2018, **1**, 300–305.
33 D. Friebel, M. W. Louie, M. Bajdich, K. E. Sanwald, Y. Cai, A. M. Wise, M.-J. Cheng, D. Sokaras, T.-C. Weng, R. Alonso-Mori, R. C. Davis, J. R. Bargar, J. K. Nørskov, A. Nilsson and A. T. Bell, *J. Am. Chem. Soc.*, 2015, **137**, 1305–1313.
34 J. T. Mefford, A. R. Akbashev, M. Kang, C. L. Bentley, W. E. Gent, H. D. Deng, D. H. Alsem, Y.-S. Yu, N. J. Salmon, D. A. Shapiro, P. R. Unwin and W. C. Chueh, *Nature*, 2021, **593**, 67–73.
35 X. Liu, L. Zhang, Y. Zheng, Z. Guo, Y. Zhu, H. Chen, F. Li, P. Liu, B. Yu, X. Wang, J. Liu, Y. Chen and M. Liu, *Adv. Sci.*, 2019, **6**, 1801898.
36 Z. Duan and G. Wang, *Phys. Chem. Chem. Phys.*, 2011, **13**, 20178–20187.
37 R. He, L. Yang, Y. Zhang, X. Wang, S. Lee, T. Zhang, L. Li, Z. Liang, J. Chen, J. Li, A. Ostovari Moghaddam, J. Llorca, M. Ibáñez, J. Arbiol, Y. Xu and A. Cabot, *Energy Storage Mater.*, 2023, **58**, 287–298.
38 J. Li, B. Li, P.-T. Li, N. Zhang and H.-S. Shang, *Rare Met.*, 2025, **44**, 1789–1799.
39 X. Cao, Y. Gao, Z. Wang, H. Zeng, Y. Song, S. Tang, L. Luo and S. Gong, *ACS Appl. Mater. Interfaces*, 2023, **15**, 32365–32375.
40 L. Luo, R. Tang, L. Su, J. Kou, X. Guo, Y. Li, X. Cao, J. Cui and S. Gong, *Energy Storage Mater.*, 2024, **72**, 103773.
41 J. Han, W. Zhang, K. Liu, H. Zheng, Y. Li, L. Luo, S. Gong, Y. Jia and X. Liang, *Appl. Surf. Sci.*, 2025, **687**, 162238.
42 M. Xie, X. Xiao, D. Wu, C. Zhen, C. Wu, W. Wang, H. Nian, F. Li, M. D. Gu and Q. Xu, *Nano Res.*, 2024, **17**, 5288–5297.
43 Q. Chen, L. Shi, G. Xu, M. Hu, M. Peng and Z. Yao, *Colloids Surf., A*, 2025, **709**, 136106.
44 C. Madan, S. R. Jha, N. K. Katiyar, A. Singh, R. Mitra, C. S. Tiwary, K. Biswas and A. Halder, *Energy Adv.*, 2023, **2**, 2055–2068.
45 Z. Jin, J. Lyu, Y.-L. Zhao, H. Li, X. Lin, G. Xie, X. Liu, J.-J. Kai and H.-J. Qiu, *ACS Mater. Lett.*, 2020, **2**, 1698–1706.
46 P. Strasser, *Acc. Chem. Res.*, 2016, **49**, 2658–2668.
47 B. Laïk, M. Richet, N. Emery, S. Bach, L. Perrière, Y. Cotrebil, V. Russier, I. Guillot and P. Dubot, *ACS Omega*, 2024, **9**, 40707–40722.
48 M. Bajdich, M. García-Mota, A. Vojvodic, J. K. Nørskov and A. T. Bell, *J. Am. Chem. Soc.*, 2013, **135**, 13521–13530.
49 C. Luan, M. Corva, U. Hagemann, H. Wang, M. Heidelmann, K. Tschulik and T. Li, *ACS Catal.*, 2023, **13**, 1400–1411.
50 J. Gallenberger, H. Moreno Fernández, A. Alkemper, M. Li, C. Tian, B. Kaiser and J. P. Hofmann, *Catal. Sci. Technol.*, 2023, **13**, 4693–4700.
51 M. C. Biesinger, B. P. Payne, A. P. Grosvenor, L. W. M. Lau, A. R. Gerson and R. S. C. Smart, *Appl. Surf. Sci.*, 2011, **257**, 2717–2730.
52 P. Patnaik, *Handbook of Inorganic Chemicals*, McGraw-Hill, New York, 2002.
53 F. Bai, J. Schulwitz, T. Priamushko, U. Hagemann, A. Kostka, M. Heidelmann, S. Cherevko, M. Muhler and T. Li, *J. Catal.*, 2024, **438**, 115697.
54 B. He, P. Hosseini, D. Escalera-López, J. Schulwitz, O. Rüdiger, U. Hagemann, M. Heidelmann, S. DeBeer, M. Muhler, S. Cherevko, K. Tschulik and T. Li, *Adv. Energy Mater.*, 2025, **15**, 2403096.
55 Z. Wang, X. Guo, J. Montoya and J. K. Nørskov, *npj Comput. Mater.*, 2020, **6**, 160.

56 R. A. Krivina, Y. Ou, Q. Xu, L. P. Twight, T. N. Stovall and S. W. Boettcher, *Acc. Mater. Res.*, 2021, **2**, 548–558.
57 A. Bergmann, E. Martinez-Moreno, D. Teschner, P. Chernev, M. Gliech, J. F. de Araújo, T. Reier, H. Dau, P. Strasser, A. Bergmann, E. Martinez-Moreno, D. Teschner, P. Chernev, M. Gliech, J. F. de Araújo, T. Reier, H. Dau and P. Strasser, *Nat. Commun.*, 2015, **6**(1), 10–12.
58 A. Bergmann, T. E. Jones, E. Martinez Moreno, D. Teschner, P. Chernev, M. Gliech, T. Reier, H. Dau and P. Strasser, *Nat. Catal.*, 2018, **1**, 711–719.
59 M. C. Biesinger, B. P. Payne, L. W. M. Lau, A. Gerson and R. S. C. Smart, *Surf. Interface Anal.*, 2009, **41**, 324–332.
60 A. Moysiadou, S. Lee, C.-S. Hsu, H. M. Chen and X. Hu, *J. Am. Chem. Soc.*, 2020, **142**, 11901–11914.

